Near-Infrared to Visible Upconversion in Er³⁺ and Yb³⁺ Codoped Lu₂O₃ Nanocrystals: Enhanced Red Color Upconversion and Three-Photon Process in Green Color Upconversion

Yanping Li,[†,‡] Jiahua Zhang,*[,†] Xia Zhang,[†] Yongshi Luo,[†] Xinguang Ren,[†] Haifeng Zhao,[†] Xiaojun Wang,[†,§] Lingdong Sun,[ǁ] and Chunhua Yan[ǁ]

Key Laboratory of Excited State Processes, Changchun Institute of Optics, Fine Mechanics and Physics, Chinese Academy of Sciences, 16 Eastern South Lake Road, Changchun 130033, People's Republic of China, Graduate School of Chinese Academy of Sciences, Beijing 100039, People's Republic of China, Department of Physics, Georgia Southern University, Statesboro, Georgia 30460, and State Key Laboratory of Rare Earth Materials Chemistry and Applications, PKU-HKU Joint Laboratory on Rare Earth Materials and Bioinorganic Chemistry, Peking University, Beijing 100871, People's Republic of China

The synthesis and upconversion luminescence properties upon a 980 nm pump of cubic $Lu_{1.88}Yb_{0.1}Er_{0.02}O_3$ nanocrystals with various shapes, e.g., nanorods, nanosheets, and nanoparticles, are studied. It is observed that with decreasing size of the nanocrystals, the relative intensity of the upconverted red emission (Er^{3+}: $^4F_{9/2} \rightarrow {}^4I_{15/2}$) to the green one ($Er^{3+}$: ($^2H_{11/2}$, $^4S_{3/2}$) $\rightarrow {}^4I_{15/2}$) is increased, and a three-photon process involved in the green upconversion, as described by $^4F_{9/2}$ (Er) + $^2F_{5/2}$ (Yb) $\rightarrow {}^2H_{9/2}$ (Er) + $^2F_{7/2}$ (Yb), is synchronously enhanced. An analysis based on steady-state rate equations indicates that the results can be induced by a large $^4I_{11/2} \rightarrow {}^4I_{13/2}$ nonradiative relaxation rate with a small $^4F_{9/2} \rightarrow {}^4I_{9/2}$ nonradiative relaxation rate. The large $^4I_{11/2} \rightarrow {}^4I_{13/2}$ nonradiative relaxation rate is attributed to the occurrence of efficient cross energy transfer to OH⁻ surface group due to the good energy match. As the size of the nanocrystals decreases, the relative surface area is increased, increasing the number of OH⁻ group that can attach to the surface, therefore, enhancing the $^4I_{11/2} \rightarrow {}^4I_{13/2}$ nonradiative relaxation rate through cross energy transfer to OH⁻ surface group.

I. Introduction

Considerable attention has been focused on ongoing research for the trivalent rare earth (RE^{3+}) ion-doped phosphors with sizes in the nanometer region. This research has been stimulated by the fact that nanocrystals doped with optically active centers have been shown to exhibit enhanced structure, electronic and optical properties.[1−5] Taking advantage of these size-induced changes, recently, near-infrared to visible upconversion luminescence in nanocrystals has attracted much interest for a variety of potential applications, such as infrared quantum counter detectors, biological medicine, optical data storage, and so on.[3−9]

The Er^{3+} ion is an ideal candidate for upconversion since its metastable levels $^4I_{9/2}$ and $^4I_{11/2}$ can be conveniently populated by commercial low-cost near-infrared laser diodes. Yb^{3+} ion is usually used as a sensitizer for increasing the absorption cross-section to enhance the upconversion efficiency.[4,9] The dynamics of the excited states of rare earth ions can be controlled by selecting different host materials.[9,10] The host materials with low phonon energy can result in a reduction of the multiphonon relaxation and thus help efficient upconversion occur. Rare earth oxides, as a promising host matrix for upconversion, possess relatively low phonon energy, favorable physical properties and high chemical durability.[4,11] During the past few years, the studies on the upconversion luminescence of Er^{3+} ion in rare earth oxides nanocrytals have been mainly focused on Y_2O_3 nanohost. Two phenomena are generally observed in the nanosystems.[4,5,12−17] One is the enhanced upconversion intensity ratio of the red emission ($^4F_{9/2} \rightarrow {}^4I_{15/2}$) to the green one (($^2H_{11/2}$, $^4S_{3/2}$) $\rightarrow {}^4I_{15/2}$), the other is the occurrence of a three-photon process in the green upconversion. However, the origin and relationship of the two phenomena have not been understood yet.

The sesquioxide Lu_2O_3 is isostructural to Y_2O_3 and crystallizes in a cubic bixbyite structure. It is observed that RE^{3+} ion-doped Lu_2O_3 exhibited stronger luminescence than the identical doped Y_2O_3. In fact, in Y-based compounds, the valence band energy levels are due predominantly to the oxygen $2p$ orbitals whereas in Lu crystals, the top of the valence band would be composed mainly of Lu $4f$ orbitals, therefore, lutetium could be a more favorable cation than yttrium for RE^{3+} ions dopant emission.[18] However, in the past few years, there were only a few papers in the literature concerning the upconversion luminescence properties of Er^{3+} singly doped Lu_2O_3 nanohost.[18,19]

In this work, we synthesized Er^{3+} and Yb^{3+} codoped Lu_2O_3 nanocrystals with various shapes, nanorods, nanosheets, and nanoparticles, by the hydrothermal approach. The dependences of the upconversion luminescence of Er^{3+} ion on the size of nanocrystals are discussed in detail. These results are compared with that of an identically doped Lu_2O_3 bulk material. Particularly, a theoretical analysis on the enhanced red upconversion and the three-photon process in the green upconversion in Lu_2O_3: Er^{3+}, Yb^{3+} nanocrytals is given. The conclusions obtained here may also apply to other Er^{3+} and Yb^{3+} codoped oxide nanocrystals.

* To whom correspondence should be addressed. E-mail: zhangjh@ciomp.ac.cn.
† Key Laboratory of Excited State Processes, Changchun Institute of Optics, Fine Mechanics and Physics, Chinese Academy of Sciences.
‡ Graduate School of Chinese Academy of Sciences.
§ Department of Physics, Georgia Southern University.
ǁ State Key Laboratory of Rare Earth Materials Chemistry and Applications, PKU-HKU Joint Laboratory on Rare Earth Materials and Bioinorganic Chemistry, Peking University.

II. Experimental Section

A. Sample Preparation. The synthesis of $Lu_{1.88}Yb_{0.1}Er_{0.02}O_3$ nanocrystals by the hydrothermal approach is described as follows: appropriate amounts of high-purity Lu_2O_3, Yb_2O_3, and Er_2O_3 powders were dissolved in dilute nitric acid, respectively, to form $Lu(NO_3)_3$, $Yb(NO_3)_3$, and $Er(NO_3)_3$ solutions. Five mol % $Yb(NO_3)_3$ and 1 mol % $Er(NO_3)_3$ solutions were added into appropriate amount of $Lu(NO_3)_3$ solution, and the mixed solution was stirred to form a homogeneous solution at room temperature. Then the pH value (pH = 7, 11, 12) of the mixed solution was adjusted by adding dropwise dilute $NH_3 \cdot H_2O$ solution. After being continuously stirred for 1 h, the milky colloidal solution was transferred into a closed Teflon-lined stainless steel autoclave with 50.0 mL capacity, and subsequently heated at 200 °C for 3 h. As the autoclave cooled to room temperature, the precipitates were washed with deionized water for several times and dried at 65 °C in a vacuum oven. The final products were obtained by annealing the precipitates at 900 °C for 1 h in air.

For comparison, the bulk $Lu_{1.88}Yb_{0.1}Er_{0.02}O_3$ material was prepared by traditional solid-state reaction method, at sintering temperature of 1500 °C for 5 h, using starting materials of Lu_2O_3, Yb_2O_3, and Er_2O_3.

B. Measurements and Characterization. The crystalline structure of samples were characterized by X-ray diffraction (XRD) (Rigaku D/max-rA power diffractometer using Cu Kα ($\lambda = 1.54178$ Å) radiation). Field emission scanning electron microscopy (FE-SEM) images were taken on S-4800 (Hitachi Company) electron microscopes. The photoluminescence (PL) spectra were measured with a Hitachi F-4500 fluorescent spectrometer. In upconversion luminescence (UCL) spectra measurement, a 980 nm diode laser was used to pump the samples, and the visible emissions were collected using the same F-4500 fluorescence spectrometer. The Fourier-transform infrared (FTIR) absorption spectra were measured by a FTS3000 FTIR spectrometer.

III. Results and Discussion

A. Morphology and Crystal Structure. In synthetic process of the hydrothermal approach, we can obtain different shapes of $Lu_{1.88}Yb_{0.1}Er_{0.02}O_3$ nanocrystals only by adjusting the pH values of the precursor solutions, as the FE-SEM images illustrated in Figure 1. When the pH is adjusted to be 7, the morphology of $Lu_{1.88}Yb_{0.1}Er_{0.02}O_3$ nanocrystals is composed of nanorods, as shown in Figure 1A. These nanorods are about 30 nm in diameter and nearly 2 μm in length. When the pH increases to 11, the morphology of nanocrystals can completely change into nanosheets, as shown in Figure 1B. Their side lengths range from 200 to 400 nm and the thickness is 30 nm or below. If the pH continuously increases to 12, then uniform nanoparticles with diameters from 10~15 nm are obtained (see Figure 1C).

Figure 2 displays the XRD patterns of all samples. The identical XRD patterns of these samples suggest the same crystal structure. All of the XRD peaks could be indexed to the cubic structure of Lu_2O_3 with space group Ia$\bar{3}$ (JCPDS No. 86−2475). Due to the size effect, the nanocrystals exhibit larger widths of the XRD peaks than the bulk one.[20] Moreover, the XRD peaks become broader and broader from nanorods to nanosheets and nanoparticles, suggesting the crystalline size decreases gradually.

B. Enhanced Red UCL in Er^{3+} and Yb^{3+} Codoped Lu_2O_3 Nanocrystals. Figure 3 shows the UCL spectra of $Lu_{1.88}Yb_{0.1}Er_{0.02}O_3$ nanorods, nanosheets, and nanoparticles under a low pump power of 20 mW at 980 nm. For comparison,
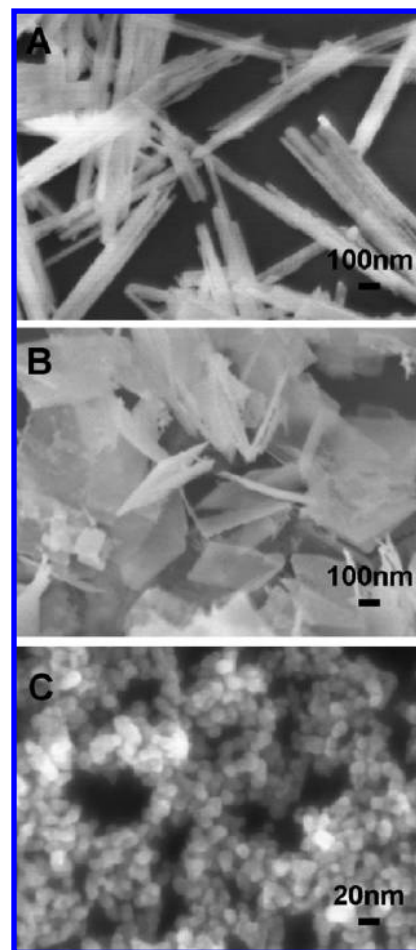
**Figure 1.** Parts A, B, and C are the FE-SEM images of $Lu_{1.88}Yb_{0.1}Er_{0.02}O_3$ nanocrystals, corresponding to pH = 7, 11, and 12, respectively.
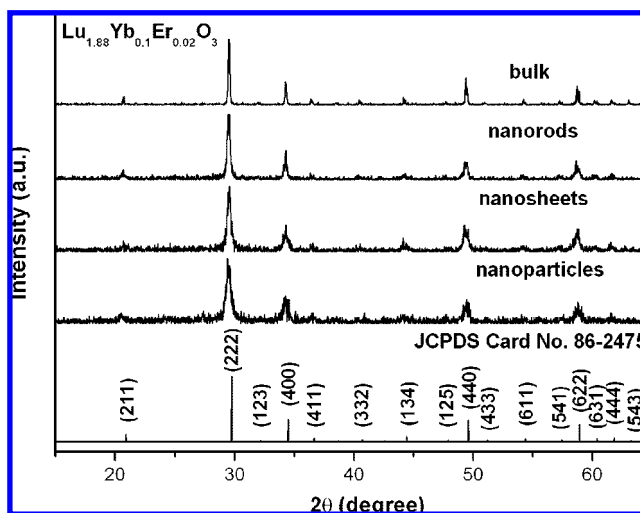
Figure 2. XRD patterns of all samples.

the UCL and the PL spectra of a $Lu_{1.88}Yb_{0.1}Er_{0.02}O_3$ bulk sample are also presented in Figure 3. The green and the red color emissions are observed in the range of 510~590 nm and 640~690 nm, respectively, corresponding to the intra $4f$-$4f$ electronic transitions ($^2H_{11/2}$, $^4S_{3/2}$) → $^4I_{15/2}$ and $^4F_{9/2}$ → $^4I_{15/2}$ of Er^{3+}. The spectra in Figure 3 have been normalized to the green emission. By comparing the UCL and the PL spectra of the bulk sample, one can find the red emission in UCL is enhanced. In the PL measurement of this work, 380 nm is selected to excite

Near-IR to Vis Upconversion in Nanocrystals

J. Phys. Chem. C, Vol. 113, No. 11, 2009 **4415**
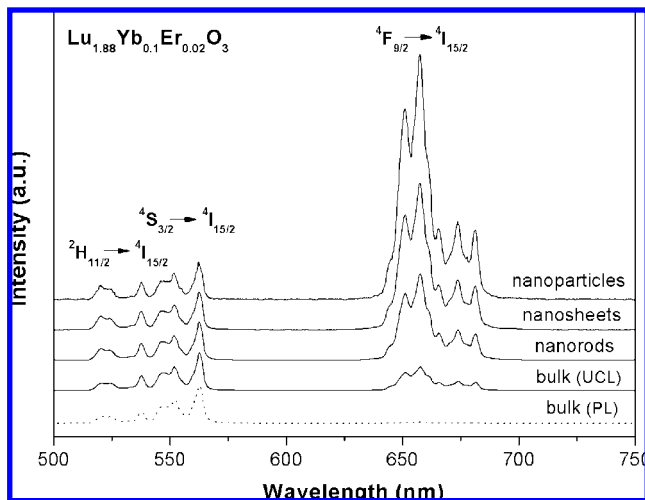
Figure 3. UCL spectra of $Lu_{1.88}Yb_{0.1}Er_{0.02}O_3$ nanocrystals and bulk (λ_{ex} = 980 nm) as well as the PL spectrum of bulk (λ_{ex} = 380 nm). Emission intensity is normalized to the $(^2H_{11/2}, {}^4S_{3/2}) \rightarrow {}^4I_{15/2}$ transition.
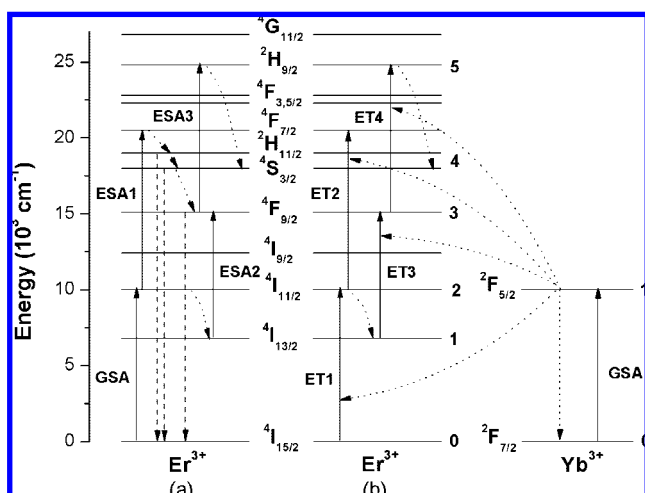
Figure 4. Energy level diagrams of Er^{3+} and Yb^{3+} ions as well as the proposed UCL mechanisms including ground-state absorption (GSA) and excited-state absorption (ESA) (a) and Yb^{3+} assistant energy transfer (ET) (b) under laser pump at 980 nm.

the $^4G_{11/2}$ level of Er^{3+}, from which the excitation subsequently relaxes down to the $^2H_{11/2}$ + $^4S_{3/2}$ levels by means of intermediate levels. In this case, the population of the red emitting $^4F_{9/2}$ level is only fed by its upper levels $^2H_{11/2}$ + $^4S_{3/2}$ through nonradiative relaxation. In contrast, the feeding of the $^4F_{9/2}$ level in UCL is performed not only by the relaxation from its upper levels, but also by two additional routes: the excited-state absorption (ESA2) from the $^4I_{13/2}$ level to the $^4F_{9/2}$ level, and an energy transfer (ET3) by assistance of Yb^{3+} described as follows: $^4I_{13/2}$ (Er) + $^2F_{5/2}$ (Yb) $\rightarrow$ $^4F_{9/2}$ (Er) + $^2F_{7/2}$ (Yb). The observation of a very strong red emission in UCL and a very weak red emission in the PL spectra indicates that the $^4F_{9/2}$ level is populated predominantly by the ESA2 and ET3 routes in UCL processes, as described by energy level diagrams in Figure 4.

In Figure 3, one can find that the red UCL in the nanosamples are much stronger than those in the bulk sample, so that the red emission dominates the UCL spectra in the nanosamples. Moreover, the red UCL relative to the green one grows up from bulk to nanorods, nanosheets, and nanoparticles. In the UCL processes, as indicated in Figure 4, the green and red UCL intensities are proportional to the population of the $^4I_{11/2}$ and
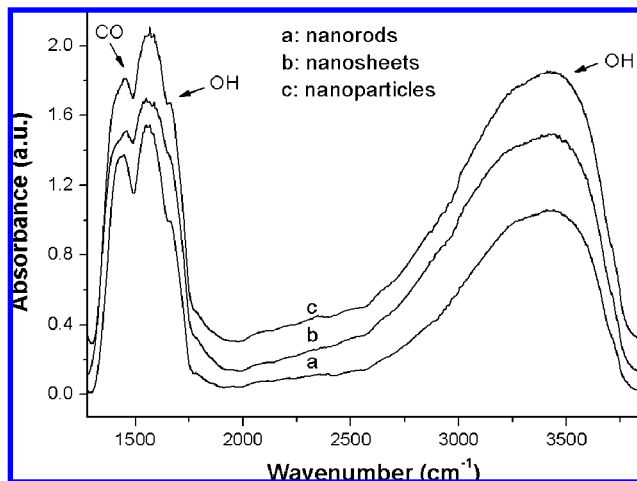
the $^4I_{13/2}$ levels, respectively. It is well-known that the populations of the two levels are strongly governed by the nonradiative relaxation from the $^4I_{11/2}$ to the $^4I_{13/2}$ levels. The population competition between the two levels can directly affect the red to green intensity ratio in UCL. Therefore, increasing the nonradiative relaxation rate can increase the population ratio of the $^4I_{13/2}$ to the $^4I_{11/2}$ levels, so as to enhance the red UCL and suppress the green UCL, simultaneously.

Figure 5 shows the FTIR spectra of $Lu_{1.88}Yb_{0.1}Er_{0.02}O_3$ nanocrystals. The bands centered at about 1650 and 3400 cm^{-1} are assigned to the characteristic vibration of OH^- groups.[16,21] Another band centered at about 1500 cm^{-1} is the vibration of the CO_3^{2-} group,[3,7] which originated from the CO_2 in the air. From the spectra, it is obvious that the intensity of the OH^- groups in nanosamples increases from nanorods to nanosheets and nanoparticles, because of the relative surface areas of the three samples are in ascending order, increasing the number of OH^- groups that can attach to the surface. On one hand, these abundant surface groups with available large vibrational quanta may efficiently enhance the multiphonon relaxation from the $^4I_{11/2}$ to the $^4I_{13/2}$ levels of Er^{3+}; On the other hand, the energy separation between the $^4I_{11/2}$ and the $^4I_{13/2}$ levels is around 3600 cm^{-1} and well matches with the hydroxyl phonon energy ($\sim$3400 cm^{-1}). The $^4I_{11/2} \rightarrow {}^4I_{13/2}$ nonradiative relaxation can be remarkably enhanced through cross energy transfer to OH^- surface group. Thus, the gradual enhancement of the red UCL from the bulk to the nanoparticles is attributed to the increasing nonradiative relaxation rate of the $^4I_{11/2}$ to the $^4I_{13/2}$ levels. A theoretical analysis of the UCL dynamical processes concerning the effect of the $^4I_{11/2}$ to $^4I_{13/2}$ nonradiative relaxation rate on the intensity ratio of the red emission to the green one is demonstrated in section D.

C. Pump Power Dependence of the UCL Intensities in $Lu_{1.88}Yb_{0.1}Er_{0.02}O_3$ Samples. To further understand the UCL mechanisms in $Lu_{1.88}Yb_{0.1}Er_{0.02}O_3$ samples, we measured the pump power dependence of the green and the red UCL intensities and plotted in a logarithmic diagram, as shown in Figure 6. For the UCL processes, the upconverted emission intensity I_{UCL} depends on the pumping laser power I_p according to the following equation:[13]

$$I_{UCL.} \propto I_p^n$$

where n is the number of pumping photons absorbed per upconverted photon emitted. On the basis of the experimental data in Figure 6, the n values for the red UCL in the bulk,

Figure 5. FTIR spectra of $Lu_{1.88}Yb_{0.1}Er_{0.02}O_3$ nanocrystals.
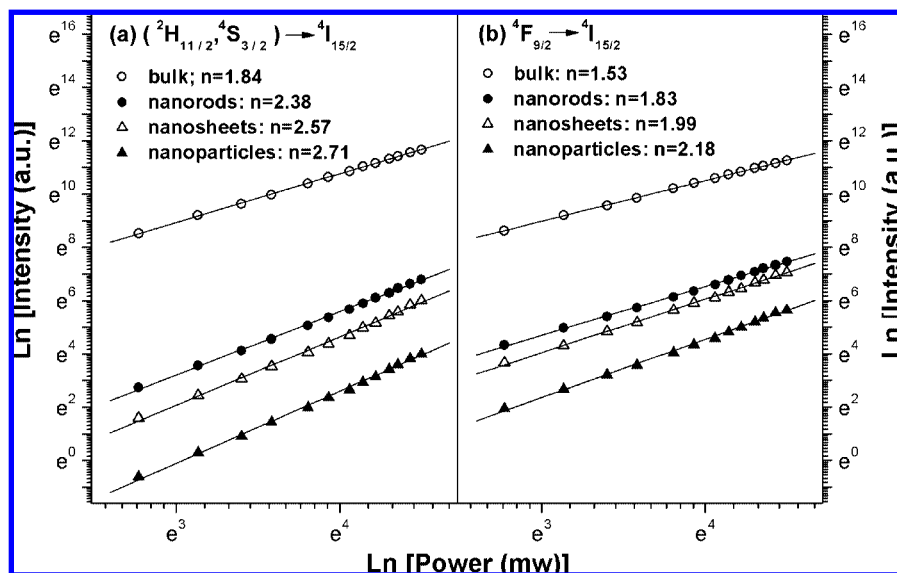
Figure 6. Power dependence of upconversion emission intensities of $Lu_{1.88}Yb_{0.1}Er_{0.02}O_3$ nanocrystals and bulk under 980 nm laser excitiation (a) $(^2H_{11/2}, {}^4S_{3/2}) \rightarrow {}^4I_{15/2}$ transition, (b) ${}^4F_{9/2} \rightarrow {}^4I_{15/2}$ transition.

nanorods, nanosheets, and nanoparticles are obtained to be 1.53, 1.83, 1.99, and 2.18, respectively, and that for the green UCL are 1.84, 2.38, 2.57, and 2.71, respectively. Obviously, the n value for the green UCL is larger than that for the red UCL in each sample, indicating a faster growth of the green UCL than the red UCL as the pump power is increased. Moreover, the n values for the green UCL are even much larger than 2 in the nanosamples, indicating a three-photon process involved in the green UCL. On the basis of the phenomenon that the n values for the green UCL increase with the increasing intensity ratios of the red emission to green, the three-photon process contributing to the green UCL is considered to be related to the red emitting level ${}^4F_{9/2}$, and described as follows: ${}^4F_{9/2}$ (Er) + ${}^2F_{5/2}$ (Yb) $\rightarrow {}^2H_{9/2}$ (Er) + ${}^2F_{7/2}$ (Yb) (ET4), as shown in Figure 4.

In the nanosamples, the dominant red emission in UCL indicates a large population of the ${}^4F_{9/2}$ level and a small population of the $(^2H_{11/2}, {}^4S_{3/2})$ levels. In this case, the third step feeding from the ${}^4F_{9/2}$ level to the $(^2H_{11/2}, {}^4S_{3/2})$ levels can remarkably increase the population of the $(^2H_{11/2}, {}^4S_{3/2})$ levels, so as to result in the n values for the green UCL higher than 2. The large population of the ${}^4F_{9/2}$ level is, thus, favorable to enhance the third photon process. Accordingly, the bulk sample mainly demonstrates a two-photon process for the green UCL with n values less than 2 due to a smaller population of the ${}^4F_{9/2}$ level, from which the red UCL is weaker than the green one from the $(^2H_{11/2}, {}^4S_{3/2})$ levels.

Figure 7a shows the descending dependence of the red to green ratio in UCL ($R/G_{(UCL)}$) on pump power. If the green to red ratio ($G/R_{(UCL)}$) is plotted as a function of pump power, then a linearly ascending trace is observed, as shown in Figure 7b. To analyze the upconverted intensity ratio as a function of the pump power is very helpful to understand the UCL mechanisms including the three-photon process involved in the green UCL.

D. Theoretical Description. To verify and make a theoretical interpretation of the results of UCL mentioned above, we utilized the following steady-state equations from the energy level diagrams presented in Figure 4:

For PL,

$$W_{43}n_4 - W_3n_3 = 0 \qquad (1)$$

For UCL,

$$W_{21}n_2 - \sigma_{13}In_1 - C_{13}n'_1n_1 - W_1n_1 = 0 \qquad (2)$$

$$W_{32}n_3 + \sigma_{02}In_0 + C_{02}n'_1n_0 - \sigma_{24}In_2 - C_{24}n'_1n_2 - W_2n_2 = 0 \qquad (3)$$

$$W_{43}n_4 + \sigma_{13}In_1 + C_{13}n'_1n_1 - \sigma_{35}In_3 - C_{35}n'_1n_3 - W_3n_3 = 0 \qquad (4)$$

$$W_{54}n_5 + \sigma_{24}In_2 + C_{24}n'_1n_2 - W_4n_4 = 0 \qquad (5)$$

$$\sigma_{35}In_3 + C_{35}n'_1n_3 - W_5n_5 = 0 \qquad (6)$$

$$\sigma'_{01}In'_0 - C_{02}n'_1n_0 - W'_1n'_1 = 0 \qquad (7)$$

where n_0, n_1, n_2, n_3, n_4, n_5 are the populations of the ${}^4I_{15/2}$, ${}^4I_{13/2}$, ${}^4I_{11/2}$, ${}^4F_{9/2}$, $(^2H_{11/2}, {}^4S_{3/2})$, and ${}^2H_{9/2}$ levels of Er^{3+}, respectively; n'_0 and n'_1 are the populations of Yb^{3+} in the ground state $(^2F_{7/2})$ and the excited state $(^2F_{5/2})$, respectively; W_{ij} is the nonradiative relaxation rate from level i to level j of Er^{3+}; W_i and W'_i are the total decay rate of level i of Er^{3+} and Yb^{3+}, respectively; σ_{ij} and σ'_{ij} are the absorption cross section between level i and level j of Er^{3+} and Yb^{3+}, respectively; C_{ij} is the energy transfer coefficient and I is the pump power.

From eq 1, the intensity ratio of the red to the green in PL is as follows:

$$R/G_{(PL)} = \gamma_3 n_3/\gamma_4 n_4 = \gamma_3 W_{43}/\gamma_4 W_3 \qquad (8)$$

Where γ_i is the radiative transition rate of level i of Er^{3+}.

From eqs 2–8, the intensity ratio of the red to the green in UCL ($R/G_{(UCL)}$) with $R/G_{(PL)}$ as a unit is written as follows:

$$R/G_{(UCL)}/(R/G_{(PL)}) = (aW_4/W_{43} + 1)/[a(\sigma_{35}I+$$
$$C_{35}bI)W_{54}/W_5W_3 + (\sigma_{35}I+C_{35}bI)/W_3 + 1] \quad (9)$$

with $a=W_{21}(\sigma_{13}+C_{13}b)/(\sigma_{24}+C_{24}b)(\sigma_{13}I+C_{13}bI+$
$$W_1) \text{ and } b = \sigma'_{01}n'_0/(C_{02}n_0+W'_1) \quad (10)$$

If $I = 0$, then the ratio in eq 9 approximately fits the situation for low pump power,

$$[R/G_{(UCL)}/(R/G_{(PL)})]_{I=0} = (W_{21}/W_1)(W_4/W_{43})(\sigma_{13}+$$
$$C_{13}b)/(\sigma_{24}+C_{24}b) + 1 \quad (11)$$

Due to $W_4 = W_{43} + \gamma_4$ and $\gamma_4 \ll W_4$, thus $W_4 \approx W_{43}$. The red to green ratio in eq 11 is, hence, mainly determined by W_{21}/W_1. As a result, the enhanced red UCL in the nanosamples, as shown in Figures 3 and 7a, is originated from the increasing of the $^4I_{11/2}$ to $^4I_{13/2}$ nonradiative relaxation rate, W_{21}. Equations 9 and 10 also describes that the $R/G_{(UCL)}/(R/G_{(PL)})$ ratio is pump power dependent. Due to the linear dependence of $G/R_{(UCL)}/(G/R_{(PL)})$ on pump power, as shown in Figure 7b, the $G/R_{(UCL)}/(G/R_{(PL)})$ ratio as a function of pump power is concentrated in the present work. In eqs 9 and 10, the lifetime $(1/W_3)$ of level 3 is observed experimentally to be as short as several tens microseconds, leading to $(\sigma_{35}I + C_{35}bI)/W_3 \ll 1$ for the pump power in this work, one has

$$G/R_{(UCL)}/(G/R_{(PL)}) = [a(\sigma_{35}I+C_{35}bI)W_{54}/W_5W_3 +$$
$$1]/(aW_4/W_{43} + 1) \quad (12)$$

It is observed in Figure 7b that the $G/R_{(UCL)}/(G/R_{(PL)})$ ratio is much less than 1. From eq 12, one has $1/(aW_4/W_{43} + 1) < [G/R_{(UCL)}/(G/R_{(PL)})] \ll 1$, leading to $1 \ll aW_4/W_{43}$, thus, eq 12 is simplified as follows:

$$G/R_{(UCL)}/(G/R_{(PL)}) = (W_{43}/W_4)\{[(W_1/W_{21})(\sigma_{24}+$$
$$C_{24}b)/(\sigma_{13}+C_{13}b)] + [(\sigma_{24}+C_{24}b)I/W_{21}] + [(W_{54}/W_5)(\sigma_{35}+$$
$$C_{35}b)I/W_3]\} \quad (13)$$

Equation 13 exhibits a linearly ascending function of pump power, identical with the results shown in Figure 7b. The first term on the right side of eq 13 is independent of pump power, describing the initial ratio; the second and the third terms are both linearly dependent on pump power. The second term is originated from the second photon process in the green UCL: ESA1 and ET2; the third term reflects the contribution of the third photon process involved in the green UCL: ESA3 and ET4. By using eq 13, the experimental data in Figure 7 can be well understood. At first, the reduction of the initial $G/R_{(UCL)}/(G/R_{(PL)})$ ratio from the bulk to the nanoparticles is the result of the increasing W_{21}, as a denominator of the first term on the right side of eq 13. At second, the reduction of the slopes for the lines from the bulk to the nanoparticles in Figure 7b is the result of the increasing W_{21} of the denominator in the second term and the increasing W_3 of the denominator in the third term. At last, the linearly ascending trace for the bulk sample is attributed to the contribution of the second term because the n value for the green UCL in the bulk sample is less than 2, not presenting the three-photon process. In contrast, the linearly ascending traces for the nanosamples are attributed to the contribution of the third term, because the n values for the green
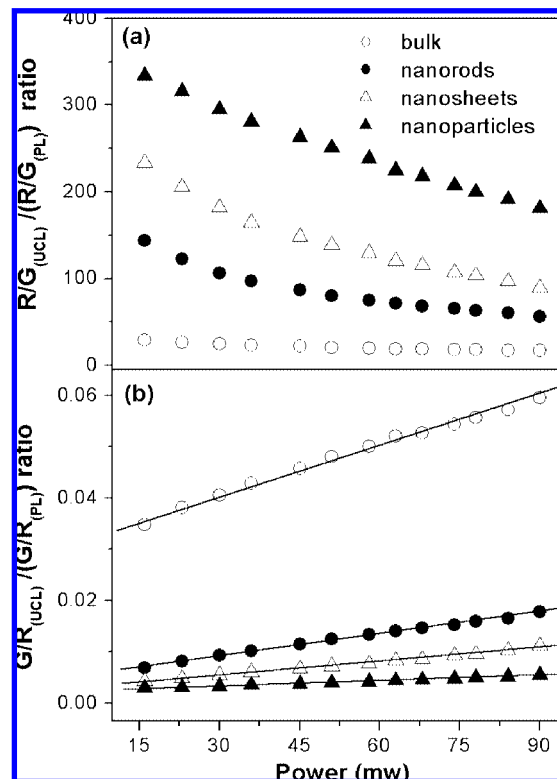

Figure 7. $R/G_{(UCL)}/(R/G_{(PL)})$ ratio (a) and $G/R_{(UCL)}/(G/R_{(PL)})$ ratio (b) of $Lu_{1.88}Yb_{0.1}Er_{0.02}O_3$ nanocrystals and bulk.

UCL are much larger than 2, demonstrating the remarkable three-photon process.

The question that needs to be answered is why the third term is much larger than the second term for the nanosamples. Regarding the high density of OH⁻ group in the nanosamples (see Figure 5), the absorption band of OH⁻ group centered at around 3400 cm⁻¹, well matches with the energy separation between the $^4I_{11/2}$ and the $^4I_{13/2}$ levels centered at around 3600 cm⁻¹. The $^4I_{11/2} \rightarrow {}^4I_{13/2}$ nonradiative relaxation is efficient through cross energy transfer to OH⁻ group. While, the depopulation of the $^4F_{9/2}$ level through cross energy transfer to OH⁻ group is comparably inefficient because the energy separation between the $^4F_{9/2}$ and the $^4I_{9/2}$ levels is around 2800 cm⁻¹, at the edge of the absorption band of OH⁻ group, not matching well with the OH⁻ group absorption. As a result, W_{21} can be much larger than W_3 in the nanosamples, making the third term much bigger than the second one.

IV. Conclusions

The cubic $Lu_{1.88}Yb_{0.1}Er_{0.02}O_3$ nanocrystals with various shapes, nanorods, nanosheets, and nanoparticles, were synthesized via adjusting the pH values of the precursor solutions in a hydrothermal approach. The upconverted red ($^4F_{9/2} \rightarrow {}^4I_{15/2}$) and green ($(^2H_{11/2}, {}^4S_{3/2}) \rightarrow {}^4I_{15/2}$) emissions are observed in both $Lu_{1.88}Yb_{0.1}Er_{0.02}O_3$ nanocrystals and bulk under 980 nm diode laser excitation. The upconverted intensity ratio of the red emission to the green one grows up from bulk to nanorods, nanosheets, and nanoparticles. Meanwhile, a three-photon process in the green upconversion occurred in the nanocrystals, which is enhanced synchronously with the increasing red emission and described as $^4F_{9/2}$ (Er) + $^2F_{5/2}$ (Yb) $\rightarrow {}^2H_{9/2}$ (Er) + $^2F_{7/2}$ (Yb) (ET4). The two correlative phenomena are induced by a large $^4I_{11/2} \rightarrow {}^4I_{13/2}$ nonradiative relaxation rate with a small $^4F_{9/2} \rightarrow {}^4I_{9/2}$ nonradiative relaxation rate. The large $^4I_{11/2} \rightarrow {}^4I_{13/2}$

nonradiative relaxation rate is induced by the efficient cross energy transfer to the OH⁻ surface group because of the good energy match with the hydroxyl phonon energy. While, the depopulation of the $^4F_{9/2}$ level through cross energy transfer to OH⁻ surface group is inefficient compared to the $^4I_{11/2} \rightarrow {}^4I_{13/2}$ nonradiative relaxation. The number of OH⁻ groups that can attach to the surface increases with decreasing the size of the nanocrystals, therefore, the $^4I_{11/2} \rightarrow {}^4I_{13/2}$ nonradiative relaxation rate is enhanced remarkably through the cross energy transfer to OH⁻ surface group, resulting in the extensive population of the red emitting level and the occurrence of the remarkable three-photon process in the green upconversion. The results herein obtained can be well understood by a theoretical analysis based on steady-state rate equations.

References and Notes

(1) Tissue, B. M. *Chem. Mater.* **1998**, *10*, 2837.

(2) Williams, D. K.; Bihari, B.; Tissue, B. M.; McHale, J. M. *J. Phys. Chem. B* **1998**, *102*, 916.

(3) Vetrone, F.; Boyer, J. C.; Capobianco, J. A.; Speghini, A.; Bettinelli, M. *J. Phys. Chem. B* **2003**, *107*, 1107.

(4) Guo, H.; Dong, N.; Yin, M.; Zhang, W. P.; Lou, L. R.; Xia, S. D. *J. Phys. Chem. B* **2004**, *108*, 19205.

(5) Lei, Y. Q.; Song, H. W.; Yang, L. M.; Yu, L. X.; Liu, Z. X.; Pan, G. H.; Bai, X.; Fan, L. B. *J. Chem. Phys.* **2005**, *123*, 174710.

(6) Lim, S. F.; Riehn, R.; Ryu, W. S.; Khanarian, N.; Tung, C.; Tank, D.; Austin, R. H. *Nano Lett.* **2006**, *6*, 169.

(7) Chen, G. Y.; Somesfalean, G.; Liu, Y.; Zhang, Z. G.; Sun, Q.; Wang, F. P. *Phys. Rev. B* **2007**, *75*, 195204.

(8) Lu, Q.; Guo, F. Y.; Sun, L.; Li, A. H.; Zhao, L. C. *J. Phys. Chem. C* **2008**, *112*, 2836.

(9) An, L. Q.; Zhang, J.; Liu, M.; Wang, S. W. *J. Alloys Compd.* **2008**, *451*, 538.

(10) Riseberg, L. A.; Moos, H. W. *Phys. Rev.* **1968**, *174*, 429.

(11) Polizzi, S.; Bucella, S.; Speghini, A.; Vetrone, F.; Naccache, R.; Boyer, J. C.; Capobianco, J. A. *Chem. Mater.* **2004**, *16*, 1330.

(12) Matsuura, D. *Appl. Phys. Lett.* **2002**, *81*, 4526.

(13) Vetrone, F.; Boyer, J. C.; Capobianco, J. A.; Speghini, A.; Bettinelli, M. *J. Appl. Phys.* **2004**, *96*, 661.

(14) Song, H. W.; Sun, B. J.; Wang, T.; Lu, S. Z.; Yang, L. M.; Chen, B. J.; Wang, X. J.; Kong, X. G. *Solid State Commun.* **2004**, *132*, 409.

(15) Pires, A. M.; Serra, O. A.; Davolos, M. R. *J. Lumin.* **2005**, *113*, 174.

(16) De, G.; Qin, W. P.; Zhang, J. S.; Zhang, J. S.; Wang, Y.; Cao, C. Y.; Cui, Y. *Solid State Commun.* **2006**, *137*, 483.

(17) Bai, X.; Song, H. W.; Pan, G. H.; Lei, Y. Q.; Wang, T.; Ren, X. G.; Lu, S. Z.; Dong, B.; Dai, Q. L.; Fan, L. B. *J. Phys. Chem. C* **2007**, *111*, 13611.

(18) Capobianco, J. A.; Vetrone, F.; Boyer, J. C.; Speghini, A.; Bettinelli, M. *Opt. Mater.* **2002**, *19*, 259.

(19) Vetrone, F.; Boyer, J. C.; Capobianco, J. A.; Speghini, A.; Bettinelli, M. *J. Phys. Chem. B* **2002**, *106*, 5622.

(20) Zhang, X. M.; Zhang, J. H.; Nie, Z. G.; Wang, M. Y.; Ren, X. G.; Wang, X. J. *Appl. Phys. Lett.* **2007**, *90*, 151911.

(21) Di, W. H.; Wang, X. J.; Chen, B. J.; Lu, S. Z.; Zhao, X. X. *J. Phys. Chem. B* **2005**, *109*, 13154.